VECTOR MAGNETIC FIELDS AND CURRENT HELICITIES IN CORONAL HOLES AND QUIET REGIONS

Shuhong Yang[1], Jun Zhang[1], Ting Li[1], and Mingde Ding[2,3]

[1] Key Laboratory of Solar Activity, National Astronomical Observatories, Chinese Academy of Sciences, Beijing 100012, China;
shuhongyang@nao.cas.cn, zjun@nao.cas.cn, liting@nao.cas.cn
[2] Department of Astronomy, Nanjing University, Nanjing 210093, China
[3] Key Laboratory for Modern Astronomy and Astrophysics (Nanjing University), Ministry of Education, Nanjing 210093, China; dmd@nju.edu.cn

ABSTRACT

In the solar photosphere, many properties of coronal holes (CHs) are not known, especially vector magnetic fields. Using observations from *Hinode*, we investigate vector magnetic fields, current densities, and current helicities in two CHs, and compare them with two normal quiet regions (QRs) for the first time. We find that the areas where large current helicities are located are mainly co-spatial with strong vertical and horizontal field elements both in shape and in location. In the CHs, horizontal magnetic fields, inclination angles, current densities, and current helicities are larger than those in the QRs. The mean vertical current density and current helicity in the CHs and QRs, averaged over all the observed areas including the CHs and QRs, are approximately 0.008 A m^{-2} and 0.005 G^2 m^{-1}, respectively. The mean current density in magnetic flux concentrations where the vertical fields are stronger than 100 G is as large as 0.012 ± 0.001 A m^{-2}, consistent with that in the flare productive active regions. Our results imply that the magnetic fields, especially the strong fields, both in the CHs and in the QRs are nonpotential.

Key words: Sun: activity – Sun: fundamental parameters – Sun: photosphere

Online-only material: color figures

1. INTRODUCTION

Coronal holes (CHs) are low density and temperature regions in the solar atmosphere (Munro & Withbroe 1972). They appear as dark areas observed with X-ray or EUV lines. CHs are always classified into three categories according to their locations and lifetimes: polar, nonpolar (isolated), and transient (Harvey & Recely 2002). In previous studies, many properties of CHs and their relationship with magnetic fields have been investigated by many authors, such as temperature variation (Wilhelm 2006; Zhang et al. 2007), element abundance (Laming & Feldman 2003), magnetic field evolution (Yang et al. 2009a, 2009b), and magnetic field structures (Meunier 2005; Zhang et al. 2006; Tian et al. 2008).

In CHs, magnetic fields are predominated by one polarity and open magnetic lines are concentrated (Bohlin 1977). Plasma escapes along the open magnetic flux, giving rise to fast solar wind (Krieger et al. 1973; Tu et al. 2005). CHs differ from the normal quiet-Sun regions mainly through a difference in magnetic structures, i.e., the field lines are mainly closed in the quiet Sun and open above CHs (Altschuler et al. 1972). Hot gas is able to escape along open field lines but is trapped in closed loops. The normal quiet Sun appears brighter due to the radiation of the trapped gas. However, the magnetic fields are not exclusively unipolar in CHs and consequently CHs should also contain locally closed coronal loops besides the open flux (Levine 1977). Wiegelmann & Solanki (2004) computed some properties of coronal loops. They found that high and long closed loops are extremely rare, whereas short and low-lying loops are almost as abundant in CHs as in the quiet Sun. This result suggests an explanation for the relatively strong chromospheric and transition region emission (many low-lying, short loops), but the weak coronal emission (few high and long loops) in CHs.

Vector magnetic fields are very significant since they can provide us with plentiful information, such as electric current and current helicity. In a common consensus, the free energy is stored in the stressed, nonpotential magnetic fields. Electric current and current helicity are two parameters which are always used to characterize magnetic nonpotentiality (Moreton & Severny 1968; Abramenko et al. 1996; Wang 1996; Zhao et al. 2009; Su et al. 2009). Electric current density J is calculated as

$$J = \frac{1}{\mu_0} \nabla \times B,$$ (1)

where μ_0 is the magnetic permeability in vacuum ($4\pi \times 10^{-3}$ G m A^{-1}). By definition, current helicity density h_c is derived as

$$h_c = B \cdot \nabla \times B.$$ (2)

The larger the deviation from the potential fields, the more energies that can power solar activity. Therefore, electric current and current helicity also serve as measures of the productivity of solar activity.

Electric current and current helicity have been intensively studied in active regions (ARs), while quantitative study is quite rare in CHs. This is mainly due to the relatively weak fields in CHs, and the former instruments are not capable of achieving reliable vector field observations. Fortunately, *Hinode* (Kosugi et al. 2007) provides us with wonderful space-based measurements which are vastly superior to previous data in resolution and sensitivity. The main purpose of this study is to compare vector magnetic fields, current densities, and current helicities in CHs and quiet regions (QRs) with *Hinode* observations. We describe the observations and data reduction in Section 2. The results are presented in Section 3, and the conclusions and discussion in Section 4.

2. OBSERVATIONS AND DATA REDUCTION

The data used here were carried out with the Spectro-Polarimeter (SP; Lites et al. 2001) in the Solar Optical Telescope
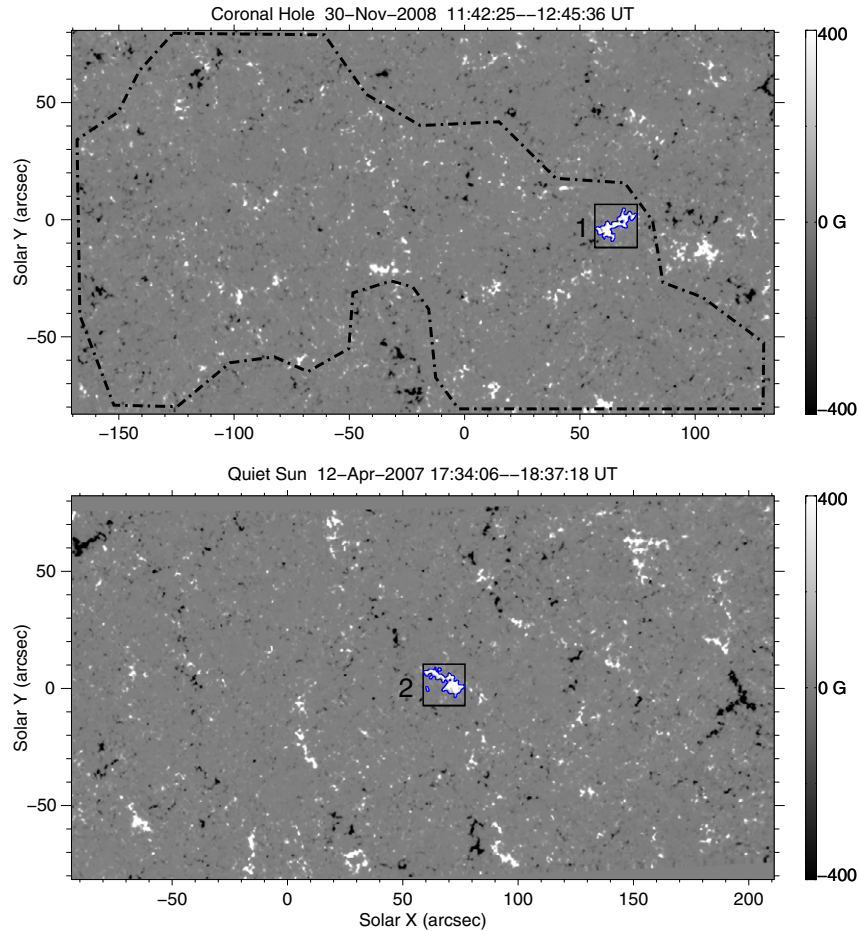
Figure 1. Overview of the vertical magnetic fields in CH1 (upper panel) and QR1 (lower panel). The dash-dotted curve delineates the CH boundary. Squares "1" and "2" outline two sub-regions that are investigated in detail. The contours in two squares are vertical magnetic fields at ±100 G levels.

(A color version of this figure is available in the online journal.)

(SOT; Ichimoto et al. 2008; Shimizu et al. 2008; Suematsu et al. 2008; Tsuneta et al. 2008) instrument aboard *Hinode*. The SP provides Stokes *I*, *Q*, *U*, and *V* profiles of two Fe lines at 630.15 nm and 630.25 nm with wavelength sampling of 21.6 mÅ in four modes (normal, fast, dynamics, and deep maps). We adopt the observations of two CHs (named CH1 and CH2 here) and two non-CH QRs (QR1 and QR2) taken in the fast map mode. For each raster slit, the integrated exposure time is 3.2 s and the pixel sampling along the slit is 0.″32. The scan is in the east–west direction with a scanning step of 0.″30. CH1 was observed from 11:42:25 UT to 12:45:36 UT on 2008 November 30, and QR1 from 17:34:06 UT to 18:37:18 UT on 2007 April 12. Both of them have a field of view (FOV) of $300'' \times 162''$. They are located almost at the disk center. CH2 was taken from 01:36:29 UT to 02:08:49 UT on 2007 November 12, and QR2 from 11:35:09 UT to 12:21:47 UT on 2007 April 13. Both of them have a FOV of $151'' \times 162''$. They are centered at about $10°$ from the disk center.

The SP data are calibrated and inverted at the Community Spectro-polarimetric Analysis Center (CSAC; http://www.csac.hao.ucar.edu/). Vector magnetic fields are retrieved using the inversion techniques based on the assumption of the Milne–Eddington atmosphere model (Kubo et al. 2007; T. Yokoyama 2010, in preparation). In the inversion, a nonlinear least-squares fitting technique is used to fit analytical Stokes profiles to the observed profiles. Values of 36 parameters are

returned from the inversion, including the three components of magnetic field (field strength B, field inclination γ, and field azimuth ϕ), the stray light fraction α, and so on. In the vector field measurements based on the Zeeman effect, there exists a $180°$ ambiguity in determining the field azimuth. Various algorithms have been developed to resolve the ambiguity, but it is also difficult to make a complete removal (Metcalf et al. 2006; Semel & Skumanich 1998). As pointed out by Metcalf et al. (2006), "the methods which minimize some measure of the vertical current density in conjunction with minimizing an approximation for the fields' divergence show the most promise." In this study, we use the improved Nonpotential Magnetic Field Calculation (NPFC) method developed by Georgoulis (2005) to disambiguate the azimuth angles.

The vector magnetic field $\boldsymbol{B}$ is shown by longitudinal field strength $B \cos \gamma$ and transverse field strength $B \sin \gamma$ without involving filling factor, where B is the intrinsic strength of the magnetic field and γ is the inclination angle with respect to the line-of-sight direction. The transverse field can be decomposed into $B_\xi = B \sin \gamma \cos \phi$ and $B_\eta = B \sin \gamma \sin \phi$ in the image plane, where ϕ is the field azimuth angle. Then, we transform the vector magnetic field at each pixel to heliographic components (B_x, B_y, B_z) according to the formulae given by Gary & Hagyard (1990). Besides, geometric mapping of the magnetograms in the image plane into the heliographic plane is also performed. Vector magnetic fields in the photosphere allow us

to compute the vertical component J_z of electric current $\mathbf{J}$ in the photospheric plane where $z = 0$. J_z, i.e.,

$$J_z(x, y, z = 0) = \frac{1}{\mu_0} \left(\frac{\partial B_y}{\partial x} - \frac{\partial B_x}{\partial y} \right) |_{z=0}, \qquad (3)$$

is calculated by finite differences. Then, we obtain the current helicity density h_c as

$$h_c(x, y, z = 0) = \mu_0 B_z J_z|_{z=0}. \qquad (4)$$

Here, h_c is just part of the current helicity density since only the vertical current density can be calculated.

We determine the noise level of vertical fields by calculating 1σ standard deviation of weak fields within intranetwork regions and find that it is about 4 G. The noise level of horizontal fields determined in a similar way is about 35 G. For current density, the noise level (0.005 A m^{-2}) is estimated from the standard deviation of them in the pixels where the horizontal fields are weaker than 35 G, similar to the method of de La Beaujardière et al. (1993), Wang et al. (1996), and Wheatland (2000). For current helicity density, the noise level (0.004 G^2 m^{-1}) is calculated from the standard deviation of them over the pixels where either the vertical or the horizontal fields are weaker than their noise levels.

3. RESULTS

CH1 and QR1 are located at the disk center, while CH2 and QR2 have nearly the same heliocentric angle. We investigate the vector magnetic fields, current densities, and current helicities of each pair of targets, respectively, and the unsigned quantities are used throughout.

3.1. Comparison between CH1 and QR1

CH1 is dominated by the positive polarity, as shown in the upper panel in Figure 1. The dash-dotted curve encloses CH1 area the pixels within which are considered only. We plot the probability density functions (PDFs) of the vertical fields in CH1 and QR1 in Figure 2 (upper panel). Not unexpectedly, CH1 fields have a generally imbalanced PDF between the positive and negative polarities. The positive fields, which are the predominant polarity, have a higher PDF than the negative. We define the magnetic flux imbalance parameter ρ as

$$\rho = \frac{\Sigma \Phi(i, j)}{\Sigma |\Phi(i, j)|}, \qquad (5)$$

where $\Phi(i, j)$ is the vertical magnetic flux at pixel (i, j). As presented in the lower panel, the flux imbalance in CH1 is about 0.65, much higher than that in QR1 (0.25). Figures 3 and 4 display the appearance of horizontal magnetic fields and the distribution of derived vertical current helicities in CH1 and QR1, respectively. When we only consider the areas where unsigned vertical magnetic fields are stronger than 4 G and horizontal fields are stronger than 35 G, the mean vertical magnetic field, horizontal field, current density, and current helicity in CH1 are 33.27 ± 0.01 G, 96.64 ± 0.07 G, 0.00888 ± 0.00001 A m^{-2}, and 0.00492 ± 0.00001 G^2 m^{-1}, while those in QR1 are 39.44 ± 0.01 G, 89.20 ± 0.06 G, 0.00839 ± 0.00001 A m^{-2}, and 0.00558 ± 0.00001 G^2 m^{-1}, respectively. Here, the uncertainties of the means are calculated according to Equation (4.14) in Bevington & Robinson (2003).
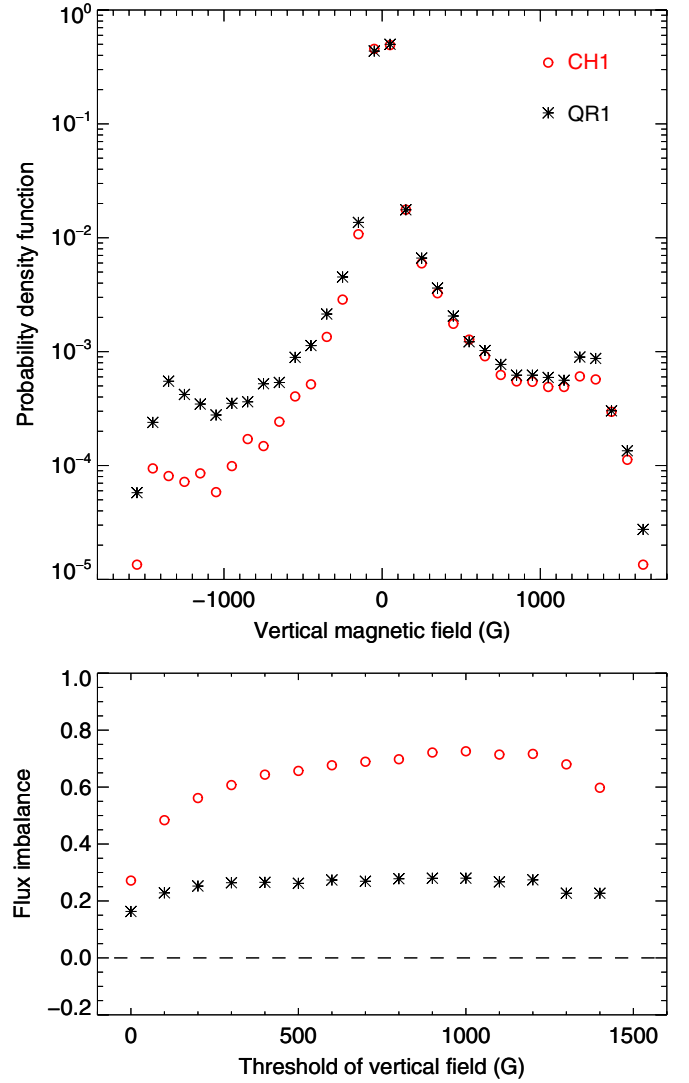

Figure 2. PDF of the vertical magnetic fields (upper panel) and flux imbalance (lower panel) in CH1 and QR1.

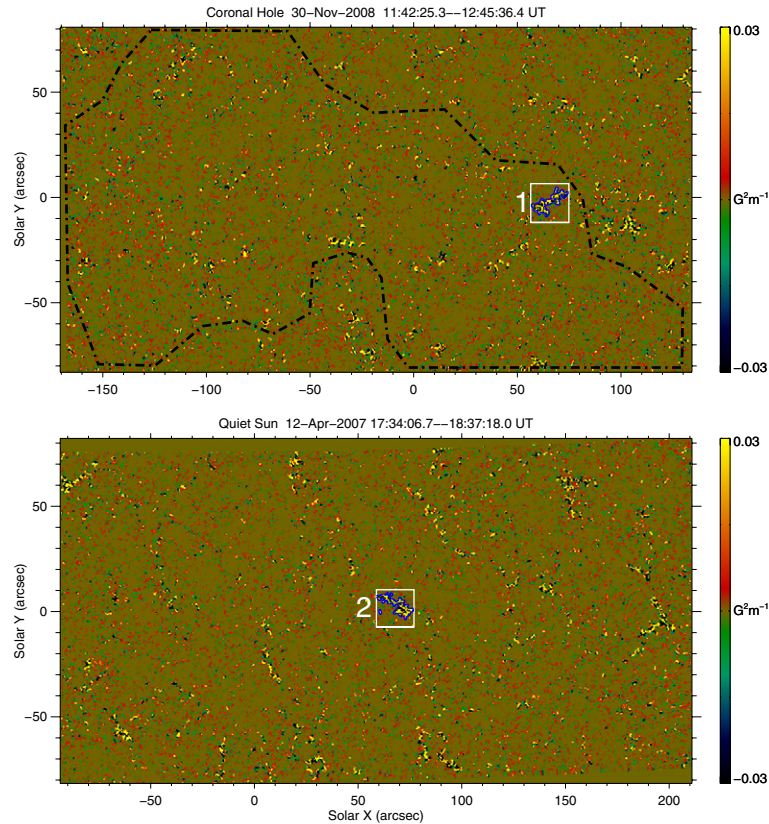(A color version of this figure is available in the online journal.)

We examine the distribution of current helicities (Figure 4) in CH1 and QR1 and find that the large current helicity concentrations are mainly co-spatial with the strong vertical and horizontal field elements (Figures 1 and 3). The region highlighted with square "1" in Figure 4 is investigated in detail. At the center of this region, large current helicities are distributed. In Figures 1–3, the contours are vertical magnetic fields at $\pm$ 100 G levels. At the places where large current helicities are located, the vertical and horizontal magnetic fields (squares "1" in Figures 1 and 3) are much stronger than the surrounding areas. We take 100 G as the general separation of strong and weak magnetic fields. The mean vertical field strength within the contour is 584.1 ± 0.2 G and the mean horizontal field strength is 162.3 ± 1.3 G. The corresponding average unsigned current density and current helicity are 0.0130 ± 0.0002 A m^{-2} and 0.0962 ± 0.0002 G^2 m^{-1}, respectively. In QR1, we select another sub-region (square "2" in Figure 4) where large current helicities are concentrated. Similar to region "1" in CH1, the areas with large current helicities also correspond with strong vertical and horizontal fields. The mean vertical field, horizontal field, electric current, and current helicity within
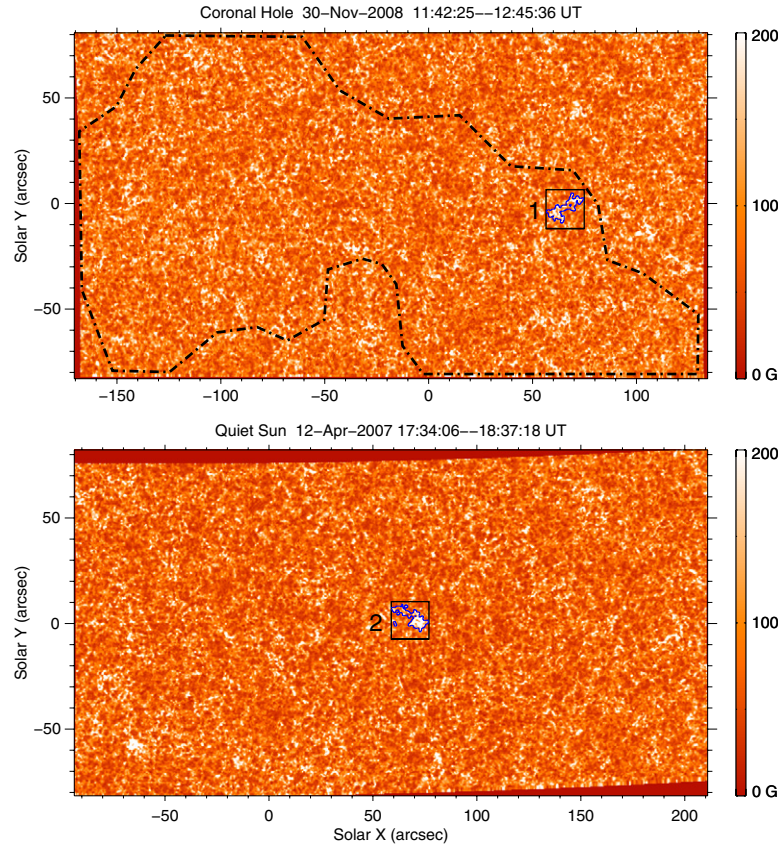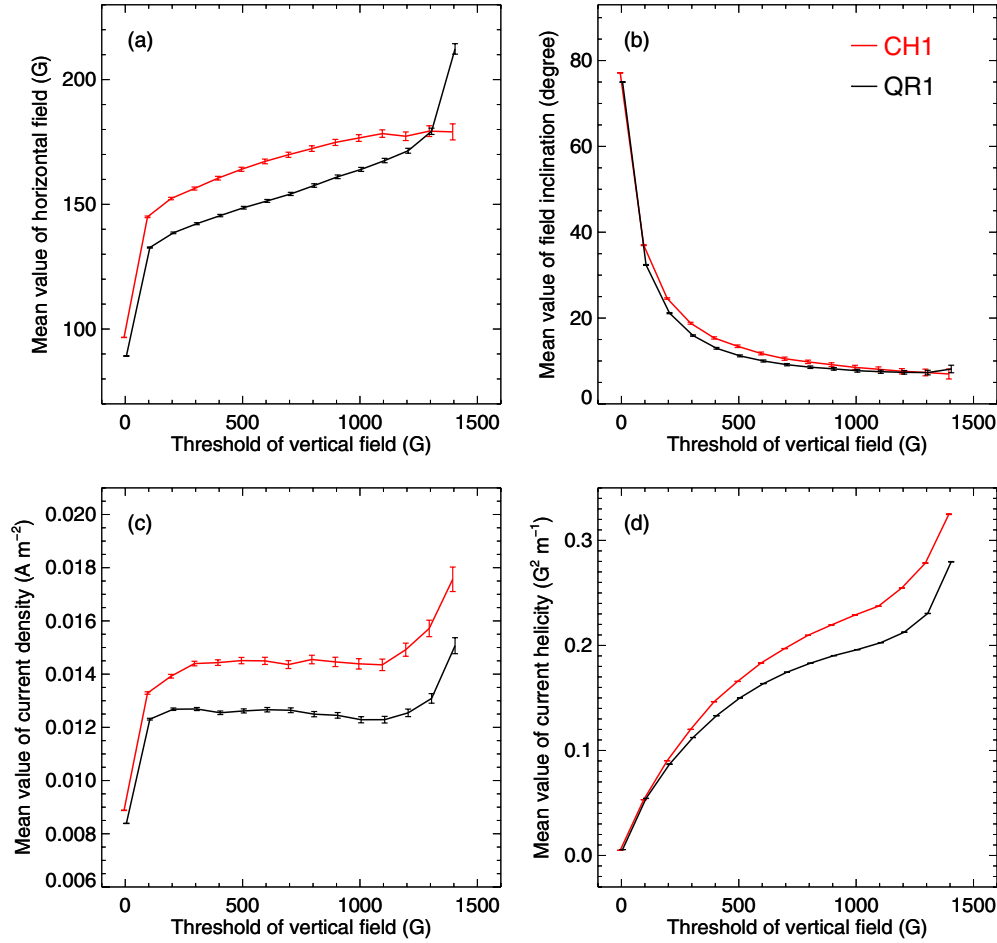
Figure 3. Appearance of the horizontal magnetic fields corresponding to Figure 1. The dash-dotted curve, squares, and contours have the same meanings as those in Figure 1.

(A color version of this figure is available in the online journal.)

Figure 4. Distribution of the vertical current helicities in CH1 and QR1. The dash-dotted curve, squares, and contours have the same meanings as those in Figure 1.

(A color version of this figure is available in the online journal.)

Figure 5. Variations of the horizontal magnetic fields (a), field inclinations (b), current densities (c), and current helicities (d) vs. the thresholds of unsigned vertical magnetic fields in CH1 and QR1. Each error bar represents the standard deviation of the mean value.

the contour curve in region "2" are 593.8 ± 0.1 G, 176.7 ± 1.3 G, 0.0131 ± 0.0002 A m^{-2}, and 0.0988 ± 0.0001 G^2 m^{-1}, respectively.

To examine whether these magnetic properties change with vertical magnetic field strength, we calculate the mean values of horizontal magnetic fields, field inclination angles, current densities, and current helicities above some thresholds of unsigned vertical magnetic fields in CH1 and QR1 (Figure 5). With the increase of thresholds from weak vertical fields to about 100 G, the mean value of horizontal fields in CH1 increases sharply from 97 G to 145 G, as shown in Figure 5(a). When the vertical fields exceed 100 G, the horizontal fields exhibit a slight increase to the level of 180 G. The relationship between vertical fields and horizontal fields in QR1 is similar to that in CH1 except for about 15 G weakness. The mean inclination angle of the magnetic lines in CH1 is about 75° for all the fields (Figure 5(b)). Then, it decreases quickly to about 38° with the increase of vertical fields in the range from weak to about 100 G. When the vertical fields are stronger than 100 G, the inclination angles gradually decrease to less than 8°, while the mean angles in QR1 are about 5° smaller than those in CH1. In CH1, the current densities increase with the vertical fields and then stay at the level of 0.014 A m^{-2}, as presented in Figure 5(c), while the average current density in QR1 is about 0.012 A m^{-2}. The difference between them is relatively significant considering their uncertainties. The current helicities in CH1 reveal a general increasing trend when the vertical fields increase from

weak fields to kilogauss (Figure 5(d)). We notice that the current helicities in QR1 exhibit similar variation trends to those in CH1 with smaller means.

3.2. Comparison between CH2 and QR2

CH2 is an enhanced network field region with a predominance of negative polarity (top left panel in Figure 6) and QR2 a normal quiet Sun with mixed polarity (top right). We also examine the PDFs of their vertical magnetic fields. Similar to those in CH1 and QR1, the PDF in CH2 is clearly asymmetric while the PDF in QR2 shows balanced positive and negative magnetic fields (upper panel in Figure 7). Compared with CH1 in Figure 2, CH2 shows a much more serious imbalance between the opposite polarities (lower panel in Figure 7). The flux imbalance ρ in CH2 is as high as −0.8 and that in QR2 is only about −0.1. The mean vertical magnetic field, horizontal field, current density, and current helicity in CH2 are 41.21 ± 0.01 G, 86.94 ± 0.07 G, 0.00808 ± 0.00001 A m^{-2}, and 0.00543 ± 0.00001 G^2 m^{-1}, while those in QR2 are 33.34 ± 0.01 G, 84.42 ± 0.08 G, 0.00796 ± 0.00001 A m^{-2}, and 0.00429 ± 0.00001 G^2 m^{-1}, respectively.

In Figure 6, the bottom panels are corresponding current helicity distributions in CH2 and QR2 scaled between ± 0.03 A m^{-2}. From their general appearance, we can see that large current helicities are also mainly co-spatial with strong magnetic fields both in shape and in location. We select two
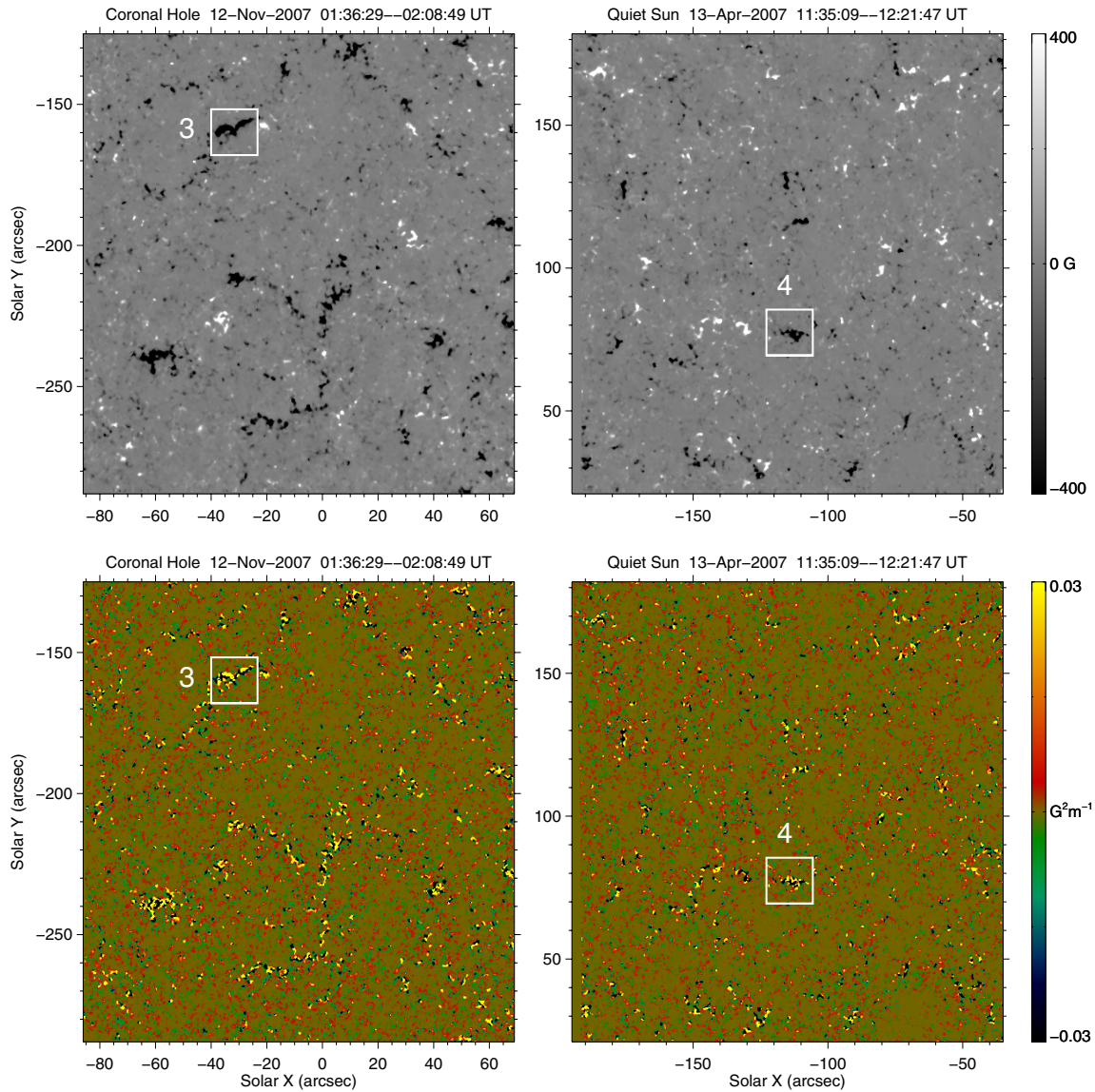
Figure 6. Vertical magnetograms in CH2 (top left) and QR2 (top right) and corresponding current helicity distributions (bottom panels). Windows "3" and "4" highlight two areas that are studied in detail.

(A color version of this figure is available in the online journal.)

areas (highlighted with windows "3" and "4") containing large current helicity patches. When we take the pixels with vertical fields stronger than 100 G into consideration, the mean vertical field strength in region "3" is as strong as 733.1 ± 0.2 G, and the mean horizontal field, current density, and current helicity are 152.8 ± 1.6 G, 0.0118 ± 0.0002 A m^{-2}, and 0.1153 ± 0.0002 G^2 m^{-1}, respectively, while these four parameters in region "4" are 511.3 ± 0.3 G, 109.0 ± 2.2 G, 0.0121 ± 0.0003 A m^{-2}, and 0.0824 ± 0.0003 G^2 m^{-1}, respectively.

We also compare the variations of horizontal fields, inclination angles, current densities, and current helicities versus the thresholds of unsigned vertical magnetic fields in CH2 and QR2. The horizontal fields increase in both CH2 and QR2 before the vertical field threshold reaches 100 G (Figure 8(a)). Then, the horizontal fields in CH2 increase slowly from 120 G to 150 G, while they mainly maintain at the 115 G level in QR2. The inclination angles in both CH2 and QR2 decrease with the increase of vertical fields in a similar trend (Figure 8(b)). The inclination angles finally approach 5°. The trend of current density variation

in CH2 is consistent with that in QR2 (Figure 8(c)). They are similar to those in CH1 and QR1 shown in Figure 5(c). When the threshold of vertical fields is several hundred gauss, the mean of current densities in CH2 is larger than that in QR2. The current helicities in both CH2 and QR2 reveal a general trend of increase when the vertical fields increase from weak fields to kilogauss though the rise slows down (Figure 8(d)). Generally, the current densities in CH2 are larger than those in QR2.

3.3. Comparison between the CHs and QRs

Figure 5 indicates that the means of the horizontal magnetic fields, inclination angles, current densities, and current helicities in CH1 are larger than those in QR1, while Figure 8 indicates that in CH2 only the horizontal magnetic fields and current helicities are stronger than QR2, and the inclination angles and current densities in them are the same for the stronger fields. To enlarge the sample, we combine two CHs (CH1 and CH2) and two QRs (QR1 and QR2), respectively. We compare the

Table 1
Mean Values and Their Uncertainties of Five Parameters in the Areas with Unsigned Vertical Magnetic Fields Stronger
than 4 G and Horizontal Fields Stronger than 35 G

Target	Vertical Field (G)	Horizontal Field (G)	Inclination (°)	Current Density (A m^{-2})	Current Helicity (G^2 m^{-1})
CH1	33.27 ± 0.01	96.64 ± 0.07	77.14 ± 0.03	0.00888 ± 0.00001	0.00492 ± 0.00001
QR1	39.44 ± 0.01	89.20 ± 0.06	74.98 ± 0.02	0.00839 ± 0.00001	0.00558 ± 0.00001
CH2	41.21 ± 0.01	86.94 ± 0.07	73.41 ± 0.03	0.00808 ± 0.00001	0.00543 ± 0.00001
QR2	33.34 ± 0.01	84.42 ± 0.08	74.93 ± 0.03	0.00796 ± 0.00001	0.00429 ± 0.00001
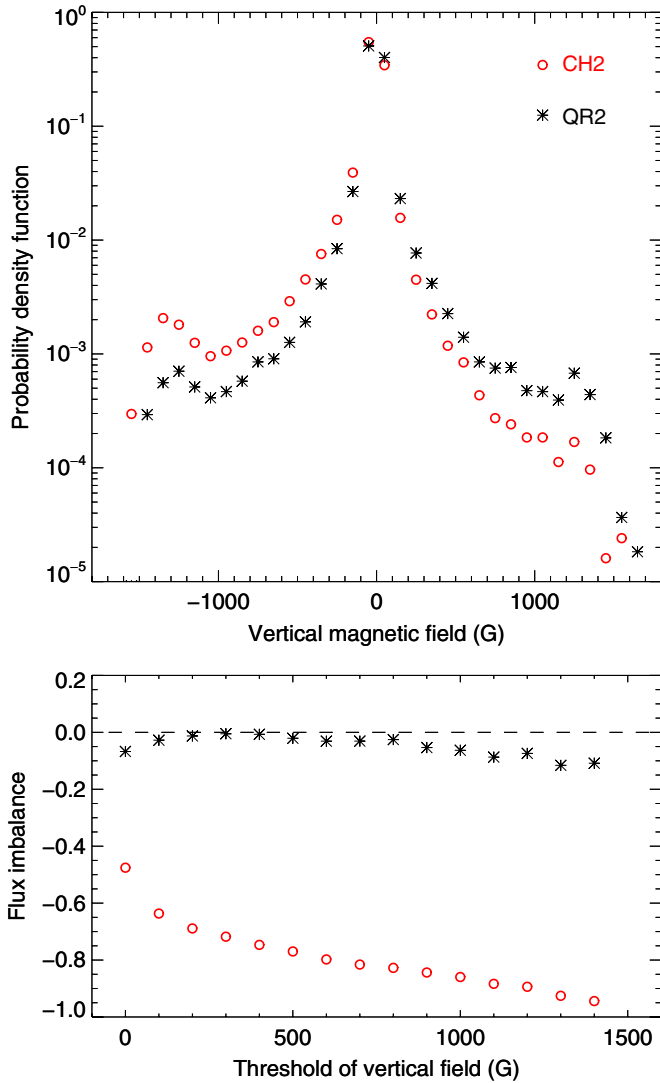
Figure 7. PDF of the vertical magnetic fields (upper panel) and flux imbalance (lower panel) in CH2 and QR2.

(A color version of this figure is available in the online journal.)

parameters between the CHs and QRs (Figure 9), and find that horizontal magnetic fields, inclination angles, current densities, and current helicities in the CHs are larger than those in the QRs.

4. CONCLUSIONS AND DISCUSSION

Using the *Hinode*/SP data, we investigate vector magnetic fields, current densities, and current helicities in two CHs (CH1 and CH2), and compare them with two QRs (QR1 and QR2).

To our knowledge, this comparison has not been done using vector field measurements before. We find that in the areas in both the CHs and in the QRs where large current helicities are concentrated, there are strong vertical and horizontal field elements and they are mainly co-spatial with each other in shape and location. In the CHs, horizontal magnetic fields, inclination angles, current densities, and current helicities are larger than those in the QRs. The mean values and their uncertainties of five parameters in the areas where the unsigned vertical magnetic fields are stronger than 4 G and horizontal fields than 35 G are listed in Table 1. Averaged over the observed CHs and QRs, the means of vertical magnetic fields, horizontal fields, inclination angles, current densities, and current helicities are approximately 37 G, 90 G, 75°, 0.008 A m^{-2}, and 0.005 G^2 m^{-1}, respectively.

The mean vertical magnetic strength in CH2 is 41 G, stronger than that in CH1 (33 G). The reason is that CH2 is located at an enhanced network region. According to the MDI Synoptic Chart, the location of CH2 is ∼250° (Carrington longitude). At the same site, there was a small mature AR on 2007 October 17, which has been studied by Murray et al. (2010). We think that the dispersion of the AR's negative polarity leads to the strong fields in CH2. The average vertical magnetic field in QR2 is 33 G, somewhat weaker than that in QR1 (39 G). It may be caused by the magnetic field fluctuation of the quiet Sun in the scale of FOV of our data. As revealed in our results, the CHs are dominated by one polarity, while magnetic fluxes in the QRs are generally balanced in sign.

There is also another way to estimate whether the difference or similarity is significant, i.e., using the uncertainties of the vector field parameters from the inversion. But this method is not available, because "some of the errors of the inversion parameters are wrong and the problem cannot be fixed any time soon," as pointed out by B. W. Lites (2010, private communication). "However, the values for the inversion parameters themselves are OK."

Flaring ARs carry more current than simple ones which are closer to potential. According to McIntosh (1990), the majority of regions are simple. As presented in our results, both in the CHs and in the QRs, large current helicity areas are almost located in the regions with strong vertical and horizontal magnetic fields. The mean current density in magnetic concentrations where the vertical fields are stronger than 100 G is as large as 0.012 ± 0.001 A m^{-2}, consistent with that (∼ 0.01 A m^{-2}) in the flare productive ARs (de La Beaujardière et al. 1993; Leka et al. 1993; Wang et al. 1994; Wang et al. 1996; Zhang 2001; Deng et al. 2001; Leka & Barnes 2003; Liu et al. 2007; Li et al. 2009). These results imply that the photospheric magnetic fields, especially the strong fields, in the CHs and QRs are nonpotential.

Since only two pairs of CHs and QRs are investigated here, more observations will be taken into consideration to check the similarities and differences between CHs and QRs.
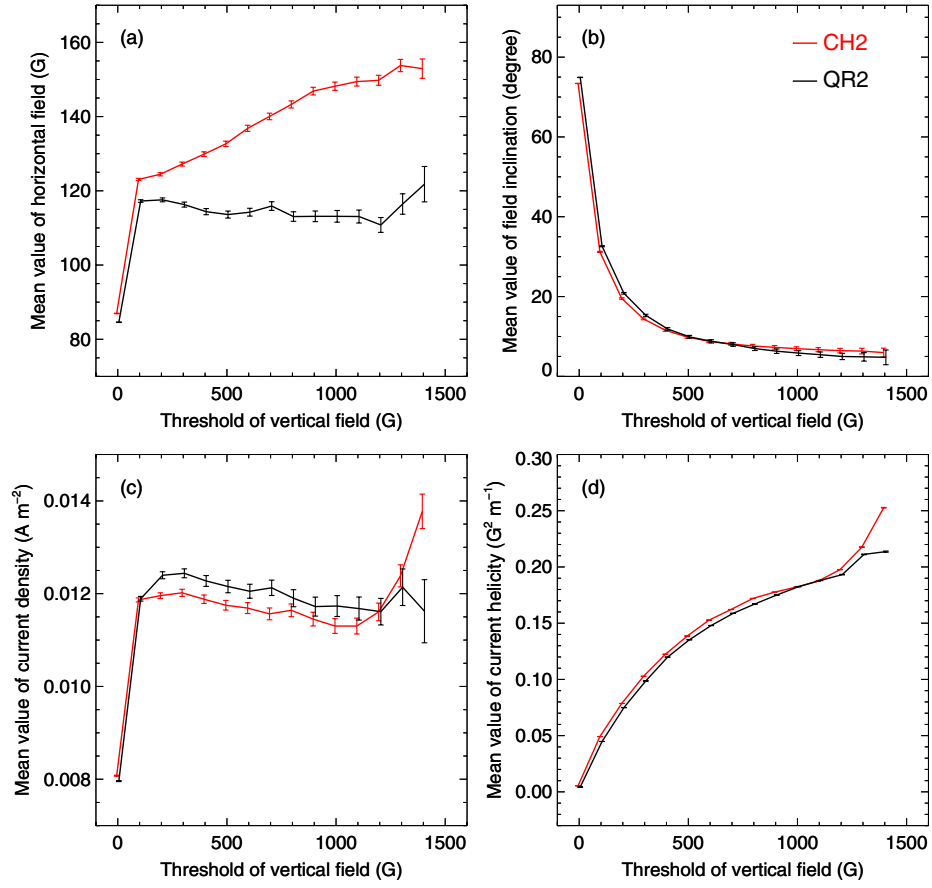
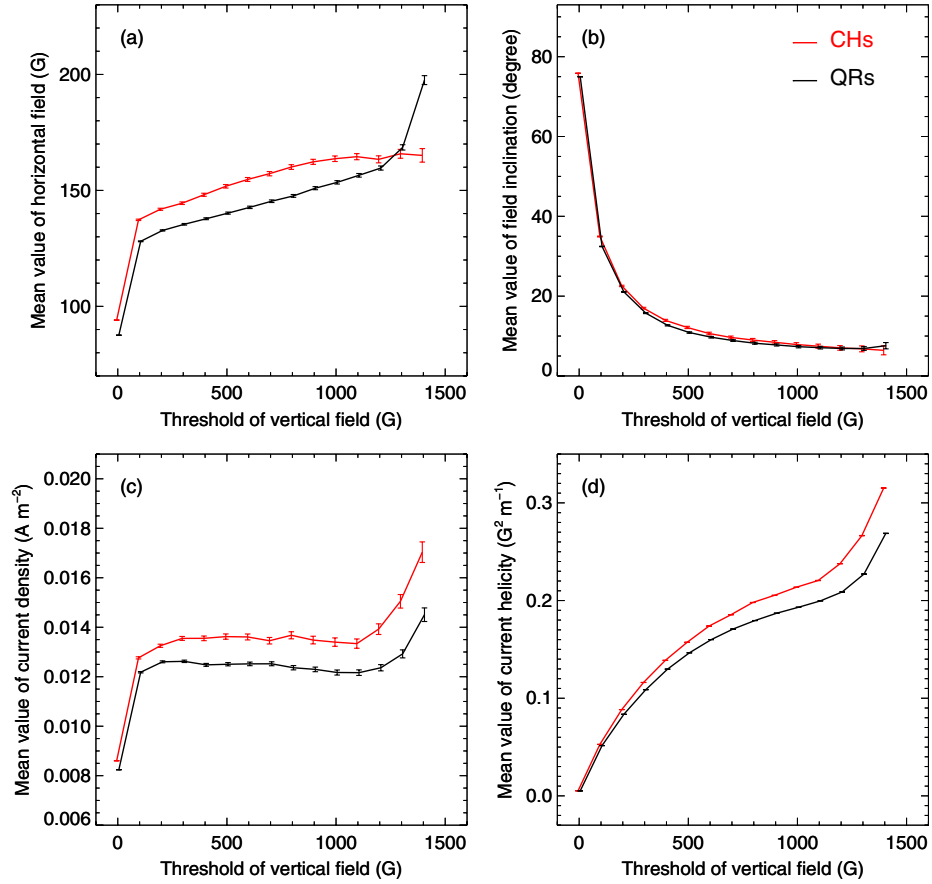**Figure 8.** Similar to Figure 5 but for CH2 and QR2.

Figure 9. Similar to Figure 5 but for the CHs (CH1 and CH2) and QRs (QR1 and QR2).

REFERENCES

Abramenko, V. I., Wang, T. J., & Yurchishin, V. B. 1996, Sol. Phys., 168, 75
Altschuler, M. D., Trotter, D. E., & Orrall, F. Q. 1972, Sol. Phys., 26, 354
Bevington, P. R., & Robinson, D. K. 2003, Data Reduction and Error Analysis for the Physical Sciences (3rd ed.; Boston, MA: McGraw-Hill)
Bohlin, J. D. 1977, Sol. Phys., 51, 377
de La Beaujardière, J. F., Canfield, R. C., & Leka, K. D. 1993, ApJ, 411, 378
Deng, Y. Y., Wang, J. X., Yan, Y. H., & Zhang, J. 2001, Sol. Phys., 204, 13
Gary, G. A., & Hagyard, M. J. 1990, Sol. Phys., 126, 21
Georgoulis, M. K. 2005, ApJ, 629, L69
Harvey, K. L., & Recely, F. 2002, Sol. Phys., 211, 31
Ichimoto, K., et al. 2008, Sol. Phys., 249, 233
Kosugi, T., et al. 2007, Sol. Phys., 243, 3
Krieger, A. S., Timothy, A. F., & Roelof, E. C. 1973, Sol. Phys., 29, 505
Kubo, M., et al. 2007, PASJ, 59, S779
Laming, J. M., & Feldman, U. 2003, ApJ, 591, 1257
Leka, K. D., & Barnes, G. 2003, ApJ, 595, 1277
Leka, K. D., et al. 1993, ApJ, 411, 370
Levine, R. H. 1977, ApJ, 218, 291
Li, J., van Ballegooijen, A. A., & Mickey, D. 2009, ApJ, 692, 1543
Lites, B. W., Elmore, D. F., & Streander, K. V. 2001, in ASP Conf. Ser. 236, Advanced Solar Polarimetry—Theory, Observation, and Instrumentation, ed. M. Sigwarth (San Francisco, CA: ASP), 33
Liu, Y., et al. 2007, Sol. Phys., 240, 253
McIntosh, P. S. 1990, Sol. Phys., 125, 251
Metcalf, T. R., et al. 2006, Sol. Phys., 237, 267
Meunier, N. 2005, A&A, 443, 309
Moreton, G. E., & Severny, A. B. 1968, Sol. Phys., 3, 282
Munro, R. H., & Withbroe, G. L. 1972, ApJ, 176, 511
Murray, M. J., Baker, D., van Driel-Gesztelyi, L., & Sun, J. 2010, Sol. Phys., 261, 253
Semel, M., & Skumanich, A. 1998, A&A, 331, 383
Shimizu, T., et al. 2008, Sol. Phys., 249, 221
Su, J. T., et al. 2009, ApJ, 697, L103
Suematsu, Y., et al. 2008, Sol. Phys., 249, 197
Tian, H., et al. 2008, A&A, 482, 267
Tsuneta, S., et al. 2008, Sol. Phys., 249, 167
Tu, C. Y., et al. 2005, Science, 308, 519
Wang, J. X. 1996, Sol. Phys., 163, 319
Wang, J. X., Shi, Z. X., Wang, H. N., & Lü, Y. P. 1996, ApJ, 456, 861
Wang, T. J., Xu, A. A., & Zhang, H. Q. 1994, Sol. Phys., 155, 99
Wheatland, M. S. 2000, ApJ, 532, 616
Wiegelmann, T., & Solanki, S. K. 2004, Sol. Phys., 225, 227
Wilhelm, K. 2006, A&A, 455, 697
Yang, S. H., Zhang, J., & Borrero, J. M. 2009a, ApJ, 703, 1012
Yang, S. H., et al. 2009b, A&A, 501, 745
Zhang, H. Q. 2001, ApJ, 557, L71
Zhang, J., Ma, J., & Wang, H. M. 2006, ApJ, 649, 464
Zhang, J., Zhou, G. P., Wang, J. X., & Wang, H. M. 2007, ApJ, 655, L113
Zhao, M., Wang, J. X., Jin, C. L., & Zhou, G. P. 2009, Res. Astron. Astrophys., 9, 933